Materials Today Physics 46 (2024) 101492

Contents lists available at ScienceDirect

Materials Today Physics

journal homepage: www.journals.elsevier.com/materials-today-physics

Charge transport dynamics and emission response in quantum-dot light-emitting diodes for next-generation high-speed displays

Jeong-Wan Jo [a,1], Yoonwoo Kim [a,1], Bo Hou [b], Sung-Min Jung [a,*], Jong Min Kim [a]

[a] Electrical Engineering Division, Department of Engineering, University of Cambridge, 9 JJ Thomson Ave, Cambridge, CB3 0FA, United Kingdom
[b] School of Physics and Astronomy, Cardiff University, 5 the Parade, Newport Road, Cardiff, Wales, CF 24 3AA, United Kingdom

ARTICLE INFO

Keywords:
Quantum-dot light-emitting diodes
Emission response
Emission intensity drop
Dynamic charge transport model
High-speed display systems

ABSTRACT

Inorganic quantum-dot light-emitting diodes (QD-LEDs) have gained significant attention as optoelectronic devices for next-generation display systems due to their superior colour properties. A comprehensive understanding of the charge transport dynamics and transient emission responses of the QD-LED is crucial to achieving high motion picture quality next-generation QD-LED display systems. In this study, we investigated the transient emission response of QD-LED devices through an advanced charge transport simulation model tailored to the quantum-dots (QDs). The dynamic response of the QD-LED devices is evaluated using the time-resolved electroluminescence measurement method for both cadmium-based and cadmium-free red, green, and blue QD-LEDs. The QD-LED devices exhibit notable emission drops during pulse voltage application. The charge transport simulation quantitatively reveals that the on and off switching speeds and the emission drops are intricately influenced by the electron and hole injection balance and a combination of carrier recombination factors within the QD layer. The charge transport simulation also shows that space-charge accumulation, due to the combined effects of charge imbalance and Auger recombination, quantitatively explains a potential device degradation mechanism. Therefore, the QD-specified charge transport model provides a crucial approach in designing and optimizing QD-LED devices for next-generation high-speed QD-LED displays with ultimate colour quality and long lifetimes.

1. Introduction

Recently, inorganic colloidal quantum-dot light-emitting diodes (QD-LEDs) have gained significant attention as optoelectronic devices for next-generation smart lighting or display systems due to their superior colour purity, colour tunability, and electrical and chemical stability [1–14]. To date, extensive research has been focused on improving the external quantum efficiency (EQE) and lifetime of the QD-LED devices, achieving over 20 % EQE along with a lifetime of 1,000,000 h [10–30]. These achievements have significantly accelerated the development of electroluminescence (EL) full-colour active matrix (AM) displays based on QD-LED with various QD patterning technologies [20–40].

Similar to other solid-state self-emissive devices such as organic light-emitting diodes (OLEDs) or gallium-nitride light-emitting diodes (GaN-LEDs), QD-LEDs show very fast emission responses due to the electron-involved carrier dynamics [41–44]. The on- and off-response characteristics seriously affect the motion picture quality in display applications [45,46]. However, these emissive devices have significant emission drops even in a single frame time, which causes unexpected brightness reduction in displaying high-speed motion pictures [47–51]. Moreover, in time-divisional volumetric displays that utilise extremely high frame rates, such as binocular stereoscopic displays, autostereoscopic displays, and depth-fused augmented reality (AR) or virtual reality (VR) displays, the slow response and emission drop of the display devices significantly degrade the three-dimensional depth cue [52–55]. Therefore, achieving fast QD-LED devices without emission drop is crucial for more vivid colour and bright high-speed motion pictures and immersive experiences in the next-generation display systems that utilise extremely high frame rates.

To achieve the fast emission response of the QD-LEDs, extensive studies of the individual material parameters and their connection to the device response time of the QD-LED are crucial. From the device perspective, the response behaviour is affected by the carrier

* Corresponding author.
E-mail address: sj569@cam.ac.uk (S.-M. Jung).
[1] These authors contributed equally: Jeong-Wan Jo and Yoonwoo Kim.

https://doi.org/10.1016/j.mtphys.2024.101492
Received 26 April 2024; Received in revised form 21 June 2024; Accepted 27 June 2024
Available online 28 June 2024

recombination processes [56–60]. However, there is a lack of detailed knowledge about device-specific carrier actions across QD-LEDs, which is essential for characterising and tailoring the emission response of the QD-LED devices. Therefore, given the complexity of physical parameters, employing computer simulations appears to be unavoidable to clearly understand the underlying physics in emission response and to achieve a fast emission response of QD-LED devices by optimizing the material and device configurations [61–68].

In this study, we investigate the dynamic emission response of QD-LEDs based on the QD-specified computational charge transport model. The experimental emission response curves are captured by the time-resolved electroluminescence (TrEL) measurement method under the external driving voltage of a square wave pulse [44,50]. The on- and off-response behaviours as well as the emission drop in a pulse period are analysed for red, green, and blue QD-LEDs fabricated in this study. To analyse the dynamic response of the QD-LED devices, we introduce a computational charge transport simulation model based on an electric field-dependent carrier injection specified for the QD-LEDs. Here, the dynamic motion of carriers and their corresponding emission responses are quantitatively analysed by the charge transport simulation for various device and material configurations to represent the charge balance conditions and the recombination processes of the QD-LED device. In the simulation, various energy band level alignment configurations are used for the charge-balanced and charge-imbalanced conditions. The carrier recombination processes such as Langevin radiative recombination process, Shockley-Read-Hall (SRH) and Auger non-radiative recombination process are also included in the simulation. Finally, the performance degradation mechanism of the QD-LED device is computationally analysed by investigating the effect of the band alignment and the recombination process on the space-charge accumulation of QD nanoparticles. This computational analysis of the transient emission response of the QD-LEDs paves the way for advancing high-speed displays based on QD-LED technology.

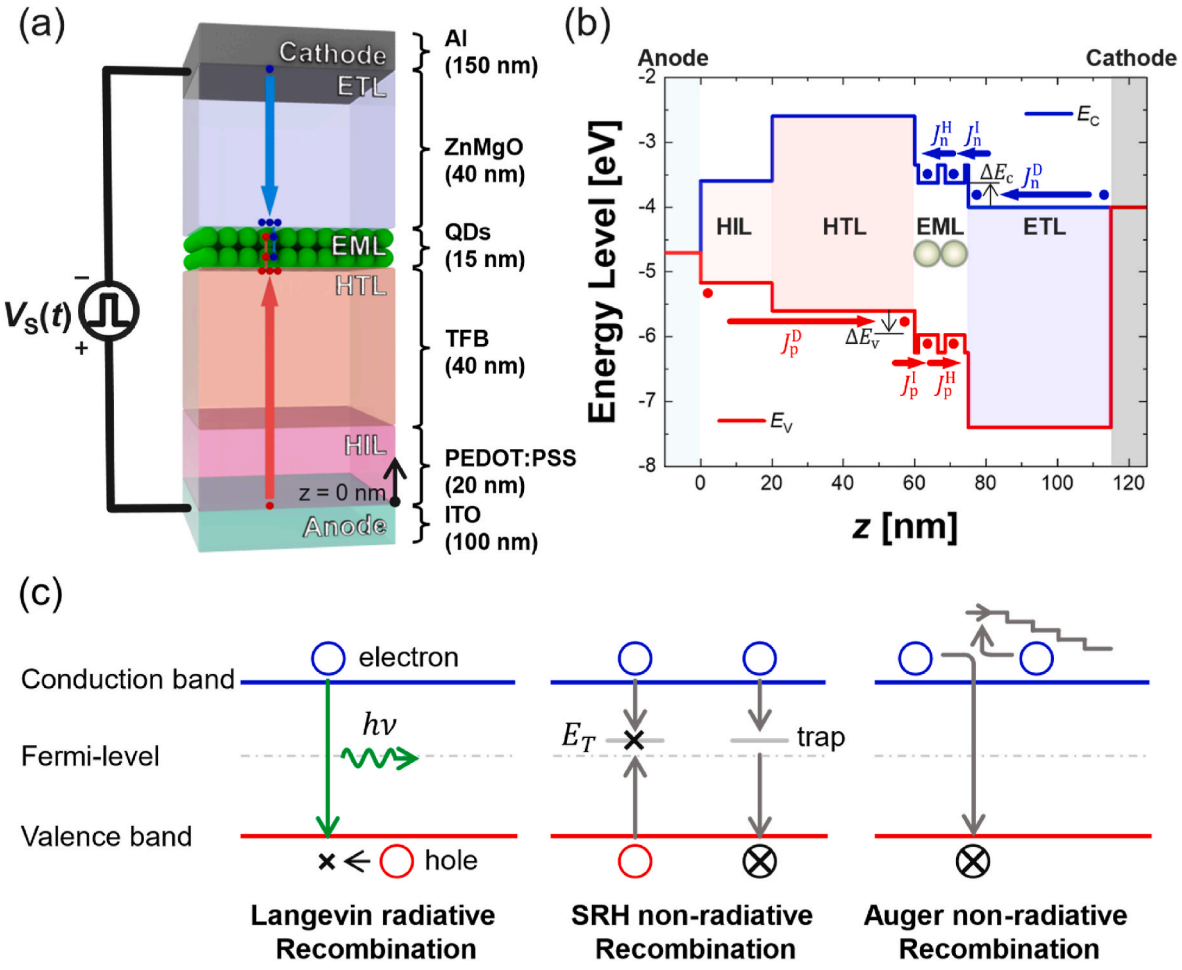

Fig. 1. Device architecture of the QD-LEDs and charge transport mechanisms. (a) Device architecture of the QD-LED device used in this study. A PEDOT:PSS, a TFB, and a ZnMgO are used for HIL, HTL, and ETL. CdSe/ZnS core/shell red, green, and blue QDs are used for the EMLs of Cd-based QD-LEDs, and InP/ZnS core/shell red and green and ZnSe/ZnS core/shell blue QDs are used for the EMLs of Cd-free QD-LEDs. ITO and Al are used for the anode and the cathode electrodes. In the simulation, the thicknesses of the HIL, HTL, and ETL are assumed to be 20 nm, 40 nm, and 40 nm, respectively. The thickness of the EML is set to 15 nm for the assumption of a bilayered QD stack with 7.5 nm QD particle size. (b) Energy-band level of each layer across the device, together with the possible current paths throughout the device. ΔE_V and ΔE_C are the band-offsets for hole and electron injection from HTL and ETL to the QD layer. The band misalignment parameter δ is defined by $\delta = \Delta E_V - \Delta E_C$. Under the assumption that all other parameters are identical for the hole and electron injection, the charge-balanced condition is indicated by $\delta = 0$ eV while the charge-imbalanced condition is indicated by $\delta > 0$ eV for electron-rich and by $\delta < 0$ eV for hole-rich conditions. The possible current flows for the hole and electron are described by the ballistic drift-diffusion current densities J_p^D and J_n^D at HIL, HTL and ETL, the carrier injection current densities J_p^I and J_n^I at the HTL/QD and QD/ETL junctions, and the carrier hopping current densities J_p^H and J_n^H between two QDs. (c) Possible carrier recombination processes including the Langevin radiative recombination process, SRH and Auger non-radiative recombination processes. (For interpretation of the references to colour in this figure legend, the reader is referred to the Web version of this article.)

2. Theory

2.1. QD-LED device architecture

Fig. 1 illustrates the device configuration of the QD-LEDs employed in both the computational charge transport simulations and the experiments. The QD-LED device is composed of a stack of multiple layers, which includes an anode electrode, a hole injection layer (HIL), a hole transport layer (HTL), an emissive layer (EML), an electron transport layer (ETL), and a cathode electrode (Fig. 1a). An indium tin oxide (ITO), poly(3,4-ethylene dioxythiophene): polystyrenesulfonate (PEDOT:PSS), poly[(9,9-dioctylfluorenyl-2,7-diyl)-co-(4,40-(N-(4-s-butylphenyl)) diphenylamine)] (TFB), QD nanoparticles, zinc magnesium oxide (ZnMgO), and aluminium (Al) are used for anode electrode, HIL, HTL, EML, ETL, and cathode electrode, respectively. Cadmium selenide (CdSe)/zinc sulphide (ZnS) core/shell QD nanoparticles are utilised for Cd-based red, green, and blue EMLs. Indium phosphide (InP)/ZnS core/shell QDs are utilised for Cd-free red and green EMLs, and zinc selenide (ZnSe)/ZnS core/shell QDs are utilised for Cd-free blue EML. A forward bias pulse voltage is applied across the anode and cathode electrodes, and the physical parameters such as electron and hole densities are simulated along the z direction perpendicular to the device plane.

2.2. QD-LED specified computational charge transport simulation model

The flat-band energy level of each layer across the entire QD-LED device is illustrated in Fig. 1b. The current densities are divided into three different current flow models: the hole and electron ballistic drift-diffusion current densities J_p^D and J_n^D within HIL/HTL and ETL, the hole and electron injection current densities J_p^I and J_n^I at the junctions between QD and the HTL or ETL, and the hole and electron hopping current densities J_p^H and J_n^H by charge exchange through the quantum tunnelling process between two neighbouring QD nanoparticles.

The spatial carrier density distribution across the device is determined by the continuity equations described in Eq. (1) [66].

$$\frac{\partial p}{\partial t} = -\frac{1}{q}\frac{\partial J_p}{\partial z} - U,$$
$$\frac{\partial n}{\partial t} = \frac{1}{q}\frac{\partial J_n}{\partial z} - U. \tag{1}$$

Here, p and n are the hole and electron densities, and q is the electric charge of a proton. J_p and J_n represent the hole and electron current densities, and U is the recombination rate per unit volume.

The electric-field-dependent hole and electron injection current densities J_p^I and J_n^I through the carrier capturing process are given by Eq. (2) [65,68].

$$J_p^I = qr_{QD}S_p\sigma T_p\mu_p^{QD}\mathscr{E}_p^{3/2}p_H(N_{QD} - p_{QD}),$$
$$J_n^I = -qr_{QD}S_{QD}\sigma T_n\mu_n^{QD}\mathscr{E}_n^{3/2}n_E(N_{QD} - n_{QD}). \tag{2}$$

Here, r_{QD} represents a radius of QD nanoparticles, and S_p and S_n are injection coefficients associated with the carrier capture cross-section for holes and electrons. σ denotes the cross-sectional area of the QD nanoparticles $\sigma = \pi \times r_{QD}^2$, and μ_p^{QD} and μ_n^{QD} stand for the mobilities of hole and electron in the QD layer, respectively. $\mathscr{E}_p$ and $\mathscr{E}_n$ denote the electric fields at the interfaces of QDs toward HTL (for hole) and ETL (for electron). These are defined as $\mathscr{E}_p = -\partial\phi/\partial z - \Delta E_V/(q \times r_{QD}) \geq 0$ and $\mathscr{E}_n = -\partial\phi/\partial z - \Delta E_C/(q \times r_{QD}) \geq 0$ at HTL/QD and QD/ETL junctions, respectively. Here, $\phi(z)$ represents the electrical potential distribution across the device, and ΔE_V and ΔE_C represent the valence and conduction band offsets at the HTL/QD and QD/ETL junctions, respectively. ΔE_V and ΔE_C are defined as $\Delta E_V = E_V^{HTL} - E_V^{QD}$ and $\Delta E_C = E_C^{QD} - E_C^{ETL}$ as illustrated in Fig. 1b. These valence and conduction band offsets, ΔE_V and ΔE_C, will be employed to configure charge balance conditions in the simulation. p_H and n_E are the hole and electron densities at the HTL/QD and ETL/QD boundaries, respectively. N_{QD} represents the density of QD nanoparticles, and p_{QD} and n_{QD} refer to the hole and electron densities at the QD layers facing the HTL and ETL, respectively.

The carrier hopping current densities, J_p^H and J_n^H, between two QDs indexed by positive integers l and m are expressed as Eq. (3).

$$J_p^H = -q\zeta_p d_{QD}(p_{QD,l} - p_{QD,m}),$$
$$J_n^H = q\zeta_n d_{QD}(n_{QD,l} - n_{QD,m}) \tag{3}$$

Here, ζ_p and ζ_n are the tunnelling coefficients of the hole and electron between two neighbouring QDs calculated from the tunnelling probability of the barrier by the shell between the cores of two QDs [68]. d_{QD} denotes the diameter of QD nanoparticles. The material parameters for the QDs used in the simulation are listed in Table S1. In the table, the diameter of the QD nanoparticles is set to be 7.5 nm with the assumption of the 5.5 nm core diameter and 1.0 nm shell thickness, for simplicity of simulation condition. However, due to the size-dependent emission wavelengths of the QD nanoparticles, the Cd-based and Cd-free red, green, and blue QD nanoparticles show different particle sizes depending on their core materials. The transmission electron microscopy (TEM) images of the CdSe/ZnS core/shell red, green, and blue (Cd-based) and InP/ZnS core/shell red and green and ZnSe/ZnS core/shell blue (Cd-free) QD nanoparticles are presented in Fig. S1.

The ballistic drift-diffusion current densities described in Eq. (4) are used for the current flow in the transport layers.

$$J_p^D = q\mu_p p\mathscr{E}_p - \mu_p k_B T\frac{\partial p}{\partial z},$$
$$J_n^D = q\mu_n n\mathscr{E}_n + \mu_n k_B T\frac{\partial n}{\partial z} \tag{4}$$

Here, μ_p and μ_n are mobilities of holes and electrons in the transport layers. k_B and T denote the Boltzmann constant and the absolute temperature of the device. $\mathscr{E}_p$ and $\mathscr{E}_n$ denote the electric fields within the transport layers derived from the electric potential field. The electric potential $\phi(z)$ is solved by the Poisson's equation given in Eq. (5).

$$\frac{\partial}{\partial z}\left(\varepsilon_r\frac{\partial\phi}{\partial z}\right) = -\frac{q}{\varepsilon_0}(p - n + N_D - N_A) \tag{5}$$

Here, ε_r and ε_0 are dielectric constants of each layer and permittivity of free space. N_D and N_A are donor and acceptor doping concentrations of each layer.

2.3. Recombination processes in the QD-LED device

The recombination processes that occur in the EML of the QD-LED device are described in Fig. 1c. The electrons and holes accumulated in QD nanoparticles undergo three recombination pathways: Langevin band-to-band radiative recombination process which generates photons [64], the SRH non-radiative recombination process involving a defective trap energy state within the bandgap in the crystal lattice [63], and the Auger non-radiative recombination process due to the crowded high-energy carriers under high bias voltages [66]. First, the bimolecular radiative recombination rate U_{RAD} is calculated by Eq. (6).

$$U_{RAD} = B(p_{QD}n_{QD} - n_i^2) \tag{6}$$

Here, B is the Langevin recombination strength and n_i is an intrinsic carrier concentration of the QD core material. SRH recombination rate U_{SRH} and Auger recombination rate U_{AUG} are used to include the non-radiative recombination processes within the device as shown in the following equations [63,66].

$$U_{SRH} = \frac{p_{QD}n_{QD} - n_i^2}{\tau_n(p_{QD} + n_i) + \tau_p(n_{QD} + n_i)} \tag{7}$$

$$U_{AUG} = \left(C_p p_{QD} + C_n n_{QD}\right)\left(p_{QD} n_{QD} - n_i^2\right) \quad (8)$$

Here, τ_p and τ_n are SRH recombination lifetimes for holes and electrons, respectively, while C_p and C_n denote the Auger recombination probabilities for holes and electrons, respectively. By assuming that the densities of holes and electrons are equal ($p_{QD} = n_{QD} = k$), which indicates a charge-balanced condition, the ambipolar equations of SRH and Auger recombination rates are derived. These equations simplify to $U_{SRH} = A(k - n_i)$ and $U_{AUG} = Ck(k^2 - n_i^2)$, where the ambipolar SRH recombination frequency is defined as $A = 1/(\tau_p+\tau_n)$ and the ambipolar Auger recombination probability C is given by $C = C_p + C_n$. Finally, the total emission intensity I_E is determined by integrating the radiative recombination rate over the entire EML region, as described by Eq. (9).

$$I_E = E_G \int_{EML} U_{RAD}\, dz \quad (9)$$

3. Material and methods

3.1. Experimental fabrication of QD-LED devices

Patterned ITO glass (ITO thickness: 100 nm) purchased from Ossila Ltd. is cleaned in acetone and isopropyl alcohol (IPA) via sonification. Following the oxygen plasma treatment, PEDOT:PSS (AI 4083, Ossila Ltd.) as HIL is spin-coated with 4,000 revolutions per minute (rpm) for 60 s and annealed at 150 °C for 10 min. TFB (in chlorobenzene, 12 mg mL^{-1}, American Dye Sources) as HTL is then spin-coated at 3,000 rpm for 60 s and annealed at 150 °C for 30 min. Cd-based QD solutions (CdSe/ZnS core/shell red, green, and blue nanoparticles in octane, 12.5 mg mL^{-1}) and Cd-free QD solutions (InP/ZnS core/shell nanoparticles for red/green and ZnSe/ZnS core/shell nanoparticles for blue in octane, 12.5 mg mL^{-1}) as EMLs are spin-coated at 3,000 rpm onto HTL surface and annealed at 100 °C for 10 min. QDs are purchased from Suzhou Xingshuo Nanotech Co., Ltd. ZnMgO nanocrystals (in butanol, 25 mg mL^{-1}) as an ETL are spin-coated onto the QD layers at 2,000 rpm and annealed at 100 °C for 10 min. Finally, Al (Testbourne Ltd.) as a cathode electrode is deposited by a thermal evaporation process under high-vacuum conditions. The devices, with an active area of 3.0 mm × 1.5 mm, are finally encapsulated within a glove box using UV-curable adhesives (Thorlabs Ltd.). All QD-LED devices were fabricated in a glove box and subjected to a positive ageing process for one week by storing the devices under controlled conditions. Additionally, the electro-optical properties such as current density, luminance curves and the EQE curves for the applied voltage ranging from 0 V to 6 V in 0.2 V increments have been measured as part of the electrical ageing process. These ageing processes allow the devices to reach a more stable state, reducing initial performance fluctuations typically observed immediately after fabrication. Following the ageing process, the time-dependent emission characteristics of the QD-LED devices were measured.

The experimental electro-optical characteristics of Cd-based and Cd-free red, green, and blue QD-LED devices, including current density - voltage - luminance curves, luminance - EQE curves, and current density - EQE curves, are plotted in Fig. S2. These figures demonstrate that the devices fabricated in this study exhibited typical device operation in EQEs and luminances for the applied voltage. In Fig. S2, the Cd-based and Cd-free red, green, and blue QD-LED devices exhibit experimental EQE droop at the high current range, indicating the presence of the Auger recombination process in the QD-LED devices [56–58,60,68].

3.2. Experimental setup for TrEL measurement

The time-dependent emission response behaviour of QD-LED devices is measured by a TrEL method depicted in Fig. S3. Fig. S3a schematically illustrates an optical setup for the TrEL measurement. A periodic square-wave pulse is applied to the device by the function generator (33220A, Agilent Technologies, Inc.), and the photons emitted from the QD-LED device are transferred to the photodiode (DET10A2, Thorlabs Ltd.) through collimation optics with the two convex lenses which are aligned with the QD-LED devices and the photodiode. The high-speed photodiode of 1 ns time resolution converts the photonic stimuli into an electrical signal, and the electrical signal is captured by an oscilloscope (HDO4104A, Teledyne Lecroy). The photograph of the experimental setup used in this study is shown in Fig. S3b.

4. Results

4.1. Experimental time-dependent emission response curves for QD-LED devices

Fig. 2 shows the experimental emission response of QD-LED devices captured using the TrEL measurement method [30,36]. To measure the time-dependent emission response, Cd-based and Cd-free red, green, and blue QD-LEDs were fabricated via a spin-coating process. Fig. 2a and b presents the normalised emission response of the Cd-based (Fig. 2a) and Cd-free (Fig. 2b) red, green, and blue QD-LED devices across several square-wave pulses. The devices are cyclically turned on for 4 ms with 6 V external voltages, operating at a 50 % pulse duty cycle, and then turned off for the subsequent 4 ms (total cycle period is 8 ms). As illustrated in the figure, emission spikes are observed immediately after the voltage is switched on. These emission spikes include the drop in emission after reaching their maximum value during the pulse duration.

The emission responses of the Cd-based red, green, and blue QD-LED devices are shown in Fig. 2c. The on-response times, defined by the transition time from 10 % to 90 % of their maximum emission, for the Cd-based red, green, and blue devices are measured to be 0.31 ms, 0.30 ms, and 0.20 ms, respectively. The blue device shows a slightly faster on-response time compared with the other colours. The off response times, defined by the transition time from 90 % to 0 % of their initial intensities, for the respective Cd-based red, green, and blue devices are also measured to be 0.34 ms, 0.36 ms, and 0.39 ms. The emission responses of the Cd-free red, green, and blue QD-LED devices are shown in Fig. 2d. The on-response times are 0.30 ms, 0.39 ms, and 0.44 ms for InP red, InP green, and ZnSe blue QD-LED devices. The off response times are 0.55 ms, 0.57 ms, and 0.58 ms for InP red, InP green, and ZnSe blue QD-LED devices. The Cd-free QD-LED devices show slightly slower response speeds compared with the Cd-based QD-LED devices.

Fig. 2e and f shows the emission intensity responses during the pulse voltage duration for the Cd-based and Cd-free QD-LEDs devices. Notably, the emission intensities for both Cd-based and Cd-free QD-LED devices reach their maximum just after the voltage application and decrease during the pulse width. These are similar behaviours previously observed in OLED operations [33–37]. In Fig. 2e, the emission intensity drop for the Cd-based QD-LED devices becomes increasingly serious in the order of red, green, and blue devices. The intensity drops from the maximum emission are measured to be 5 % for red, 18 % for green, and 54 % for blue devices during a 4 ms pulse duration. In contrast, the intensity drop for the Cd-free QD-LED devices becomes more serious in the order of blue, green, and red devices as shown in Fig. 2f. The intensity drops for Cd-free red, green, and blue devices are 24 %, 15 %, and 7 %, respectively, during the same pulse duration. The response characteristics for Cd-based and Cd-free red, green, and blue QD-LED devices with their maximum EQEs are summarised in Table 1. The recombination parameters affect both the response characteristics and the EQE of the QD-LED devices, simultaneously. However, the optical efficiency determined by the layered structure of the device and the optical properties of QD materials affects only the device EQE. Therefore, a direct relationship between the response characteristics and the EQE of the device is hardly observed in our experiments.

The discrepancy in emission responses, especially for the emission intensity drop and the time to reach their maximum intensity, is attributed to the differences in the charge injection between the hole and

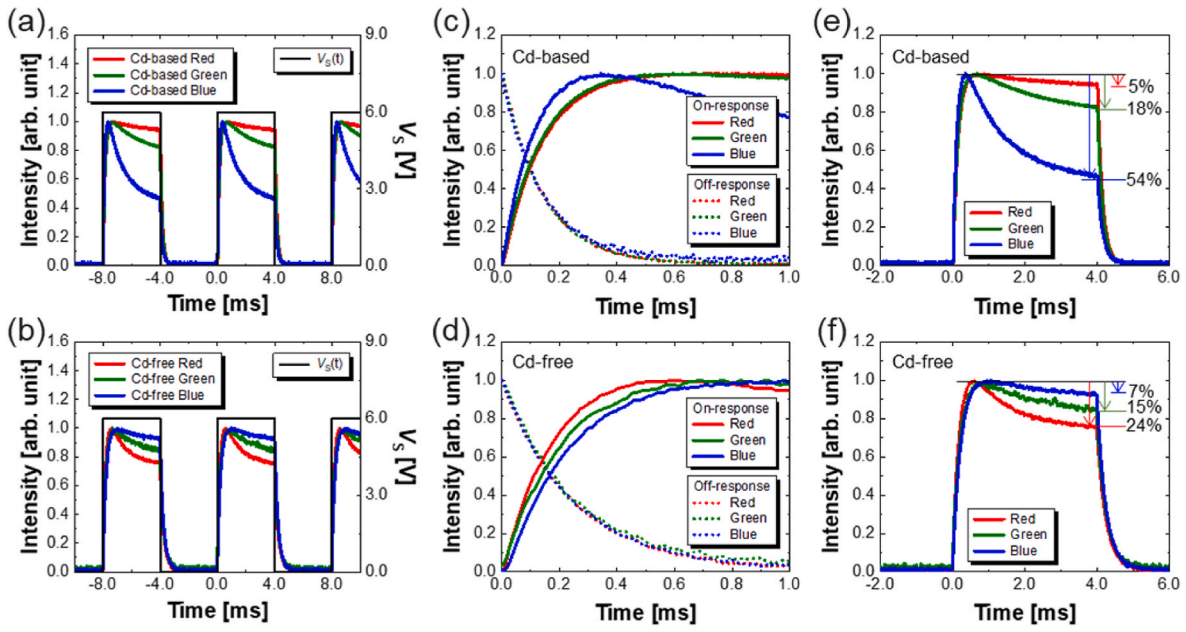

Fig. 2. Experimental emission response of QD-LED devices captured by the TrEL measurement method. Normalised transient emission response curves of (a) the Cd-based red, green, and blue QD-LED devices and (b) the Cd-free red, green, and blue QD-LED devices for a given pulse voltage. The device is switched on with 6 V external voltages for 4 ms as a 50 % duty cycle and switched off for the next 4 ms, periodically with 125 Hz frequency (one period time is 8 ms). On and off responses of (c) Cd-based red, green, and blue devices and (d) Cd-free red, green, and blue devices. The on-response times of the Cd-based red, green, and blue devices are 0.31 ms, 0.30 ms, and 0.20 ms, respectively, while the off-response times are 0.34 ms, 0.36 ms, and 0.39 ms for the respective devices. The on-response times of the Cd-free red, green, and blue devices are 0.30 ms, 0.39 ms, and 0.44 ms, respectively, while the off-response times are 0.55 ms, 0.57 ms, and 0.58 ms for the respective devices. The emission drop during the pulse width is observed for both (e) Cd-based and (f) Cd-free QD-LEDs across the colours. The emission drops from their initial intensities for the Cd-based red, green, and blue QD-LED devices are 5 %, 18 %, and 54 %, respectively. The emission drop from their initial intensity for the Cd-free red, green, and blue QD-LED devices are 24 %, 15 %, and 7 %, which is the opposite behaviour compared to the Cd-based QD-LED devices. (For interpretation of the references to colour in this figure legend, the reader is referred to the Web version of this article.)

Table 1
Experimental response times and emission drops in various QD-LED devices with the maximum EQEs.

Parameters	Cd-based QD-LEDs			Cd-free QD-LEDs		
	CdSe/ZnS Red	CdSe/ZnS Green	CdSe/ZnS Blue	InP/ZnS Red	InP/ZnS Green	ZnSe/ZnS Blue
Maximum EQE [%]	9.6	8.0	1.2	3.6	0.9	2.3
On response time [ms]	0.31	0.30	0.20	0.30	0.39	0.44
Off response time [ms]	0.34	0.36	0.39	0.55	0.57	0.58
Emission drop [%]	5	18	54	24	15	7

electron and the carrier recombination properties of the QD layers [44]. From our experiment, the emission drop of the Cd-based QD-LED devices increases as the colour changes from red and green to blue. In contrast, the emission drop of the Cd-free QD-LED devices becomes larger as the colour changes from blue and green to red (Fig. 2f). One of the reasons is that Cd-based and Cd-free QDs have different energy level configurations as the optical energy band gap increases according to the red, green, and blue colours. These emission intensity drops cause unexpected brightness reduction in displaying high-speed motion pictures in display applications, which requires the compensatory over-driving signal scheme for the one-pixel driving thin-film transistor (TFT) circuits [47]. The differences in electro-optical responses for the colours will also distort the original colours in displaying high-speed motion pictures, requiring more sophisticated optimisation of signal schemes for each colour depending on the QD colour [49]. The electro-optical response characteristics, including on/off-response times and emission intensity drop of the QD-LED device will be quantitatively analysed in the following sections by the QD-specified computational simulation model.

4.2. Off response of device emission by carrier recombination

First, the off response of the QD-LED devices is analysed by a simplified carrier decay model. Assuming that there is no carrier injection or leakages after the voltage is switched off, electrons and holes accumulated in QD nanoparticles decay only through the carrier recombination process. Considering the charge-balanced condition in which the electron and hole densities at QDs, n_{QD} and p_{QD}, are completely equal to k ($n_{QD} = p_{QD} = k$), the equation for time-dependent carrier density decay at QD is simplified from Eqs. (1)–(8) to Eq. (11).

$$\frac{\partial k}{\partial t} = -Ak - Bk^2 - Ck^3 \tag{11}$$

Here, the intrinsic carrier concentration n_i is neglected since $k \gg n_i$. When more than two recombination processes undergo simultaneously, Eq. (11) can only be solved by a numerical integration method in the time domain with the initial carrier density k_0.

Fig. 3 shows the time-dependent carrier density decay at the QD layer and their emission intensities under various combinations of A, B, and C parameters after switching off the voltage. Fig. 3a and b shows the time-dependent carrier density and emission intensity for the different Langevin recombination strengths B when the SRH and Auger recombination processes are neglected (i.e., $A = 0\ s^{-1}$ and $C = 0.0\ cm^6\ s^{-1}$). As the Langevin recombination strength increases, a faster decay of the carrier density is observed (Fig. 3a). The off response time is approximately 0.2 ms when $B = 10^{-14}\ cm^3\ s^{-1}$, closely matching the experimental off response time (Fig. 3b). Fig. 3c and d presents the time-

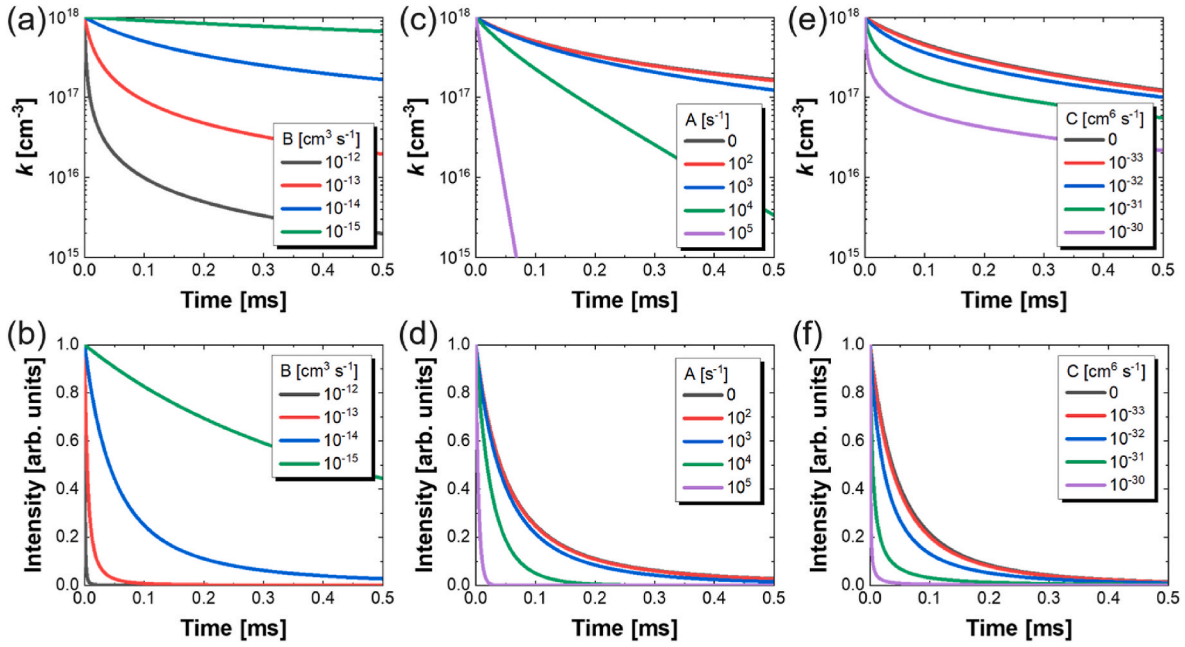

Fig. 3. Time-dependent carrier decay at the QD layer and its emission intensity under various combinations of Langevin radiative recombination strength B, SRH recombination frequency A, and Auger recombination probability C after switching off the voltage. (a) The carrier density decay and (b) intensity decay for the different Langevin recombination strengths B when the SRH and Auger recombination processes are excluded ($A = 0$ s^{-1} and $C = 0.0$ cm^6 s^{-1}). (c) The carrier density decay and (d) intensity decay according to the SRH recombination frequency A ($B = 10^{-14}$ cm^3 s^{-1} and $C = 0$ cm^6 s^{-1}). The time-dependent (e) carrier decay and (f) intensity decay for different Auger recombination probability C ($B = 10^{-14}$ cm^3 s^{-1} and $A = 10^3$ s^{-1}). The major factor determining the off-response characteristics is the combination of recombination parameters. For the experimental off responses around 0.3 ms given in Fig. 2, the B, A, and C parameters are inferred to be $A = 10^3$ s^{-1}, $B = 10^{-14}$ cm^3 s^{-1}, and $C = 10^{-32}$ cm^6 s^{-1}, respectively, in this study for the full time-dependent charge transport simulation model.

dependent carrier density and emission intensity according to the SRH recombination frequency A when $B = 10^{-14}$ cm^3 s^{-1} and $C = 0$ cm^6 s^{-1}. As A increases, the carrier density decays more quickly (Fig. 3c), and a more rapid decrease in emission intensity is observed (Fig. 3d). Considering the experimental off-response time of around 0.3 ms, it is guessed that A can be chosen to be at least less than 10^3 s^{-1} from the simulation. The time-dependent carrier density only by the SRH recombination process (where $B = 0$ cm^3 s^{-1} and $C = 0$ cm^6 s^{-1}) is given in Fig. S4a for comparison.

The time-dependent carrier density and emission intensity for different Auger recombination probability C, when $B = 10^{-14}$ cm^3 s^{-1} and $A = 10^3$ s^{-1}, are presented in Fig. 3e and f. Carrier density decays rapidly when the Auger recombination probability exceeds 10^{-31} cm^6 s^{-1} (Fig. 3e), and the off response time of emission intensity is around 0.2 ms for C less than10^{-32} cm^6 s^{-1} (Fig. 3f). The time-dependent carrier density only by the Auger recombination process (where A and B are both neglected) is given in Fig. S4b for comparison. The recombination rates for the condition of $A = 10^3$ s^{-1}, $B = 10^{-14}$ cm^3 s^{-1}, and $C = 10^{-32}$ cm^6 s^{-1} are plotted in Fig. S4c. Langevin radiative recombination predominates across the entire time domain. However, Auger recombination predominates immediately after the switch-off (when carrier density is high), and SRH recombination surpasses Auger recombination as the carrier density decreases. Through the simplified time-dependent carrier decay model, it is confirmed that the major factors determining the off-response characteristics are the combination of recombination parameters. To achieve enhanced off-response time, it is required to have higher Langevin recombination strength with higher SRH and Auger recombination parameters. Nevertheless, since the SRH and Auger recombination process deteriorates the device EQEs [57–60], an exceptionally high Langevin recombination strength with low SRH and Auger recombination parameters is crucial, despite the positive impact of the SRH and Auger parameters on the off response time of QD-LED devices.

This can be achieved by adjusting SRH and Auger parameters by careful selection of QD materials and optimisation of their process conditions. In detail, since the non-radiative SRH recombination diminishes the EQE of the device, careful selection of core and shell materials, as well as QD synthesis methods, is crucial. This enables lower SRH recombination rates in QDs by minimizing trap sites caused by lattice mismatches at the core/shell interfaces. Additionally, since non-radiative Auger recombination also reduces the EQE, choosing materials with lower dielectric constants and designing QD structures are vital to minimizing Auger recombination probabilities. However, given that dielectric constants and QD core radius directly influence the optical energy bandgap of QDs, a balanced optimisation between minimizing Auger recombination probability and maintaining the desired optical energy bandgap is necessary [69,70].

4.3. Computational simulation of carrier dynamics in QD-LED devices

To observe the impact of the carrier mobilities of the transport layers on the dynamic emission response of the QD-LED devices, the on- and off-response characteristics for different carrier mobilities of the HTL and ETL are simulated by the QD-specified charge transport model. Fig. 4 shows the dynamic carrier distribution across the device and the variation of emission intensity over time for different carrier mobilities of the HTL and ETL. The voltage is switched on to 5 V at 0.01 ms and switched off to 0 V at 0.51 ms for the duty duration of 0.5 ms. Here, charge injection coefficients for hole and electron S_p and S_n are identically set to 0.5 for charge-balanced conditions. The material and device parameters for the QDs and the transport layers used in the simulation are listed in Tables S1 and S2.

The dynamic behaviour of electron and hole carrier distributions for $\mu_p^{HTL} = \mu_n^{ETL} = 10^{-3}$ cm^2 V^{-1} s^{-1} (in Eq. (3)) is presented in Fig. 4a and b. When the voltage is switched on (Fig. 4a), the holes and electrons at the boundary of the HTL and ETL facing the QD layer quickly accumulate within 10 μs due to the high carrier mobility of the transport layers. Meanwhile, the carriers at the QD layer are accumulated relatively

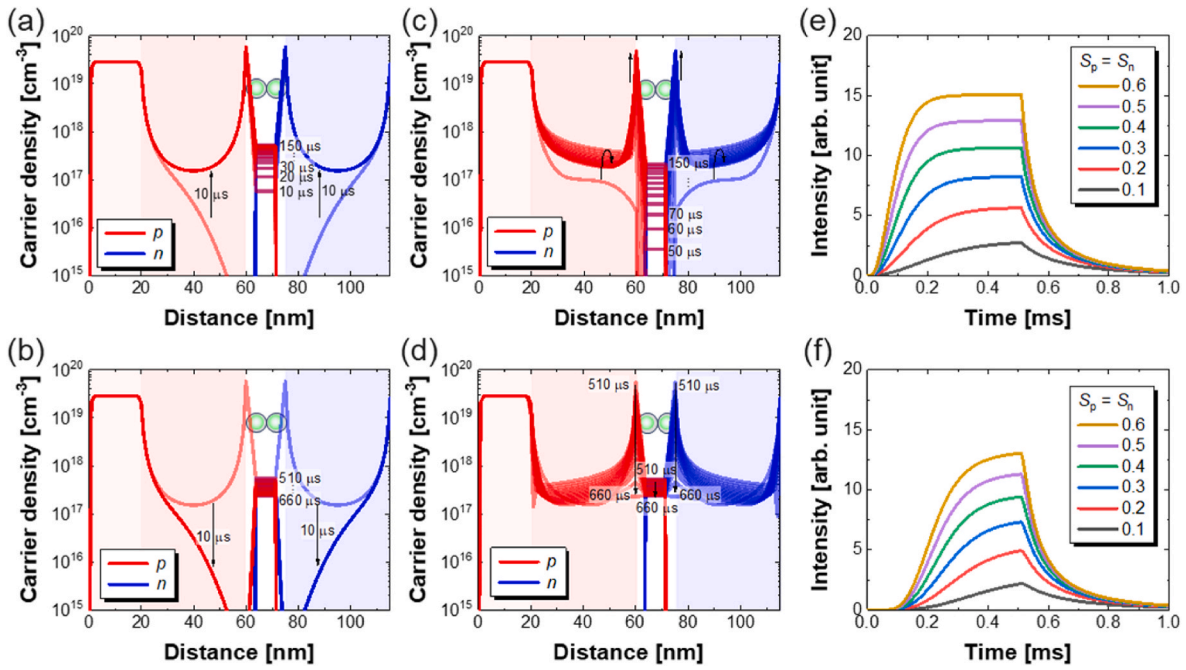

Fig. 4. Dynamic carrier distribution across the device and the variation of emission intensity over time for different carrier mobilities of the HTL and ETL under the charge-balanced condition. Hole and electron distributions after (a) switching on and (b) switching off when the carrier mobility of the ETL and HTL is equal to 10^{-3} cm^2 V^{-1} s^{-1}. Hole and electron distribution after (c) switching on and (d) switching off when the carrier mobility of the ETL and HTL is equal to 10^{-6} cm^2 V^{-1} s^{-1}. The simulated emission intensity over time for different charge injection coefficients under a charge-balanced condition ($S_p = S_n$) at HTL and ETL carrier mobilities of (e) 10^{-3} cm^2 V^{-1} s^{-1} and (f) 10^{-6} cm^2 V^{-1} s^{-1}. When the mobility of the transport layer is high enough (10^{-3} cm^2 V^{-1} s^{-1}), faster response time with higher intensity is observed as the charge injection coefficient increases. The same behaviour is observed when the mobility of the transport layer is low (10^{-6} cm^2 V^{-1} s^{-1}). The response delay at the on response due to the slow accumulation of the carriers at the HTL/QD and QD/ETL boundaries is observed when the mobility of the transport layer is low.

slowly, balancing between the carrier injection and the recombination processes in the QD layer. When the voltage is switched off (Fig. 4b), the boundary carriers in the transport layers deplete rapidly. However, the carriers at the QD layer decay slowly regardless of the rapid depletion of HTL and ETL boundary carriers. This is because the carrier decay after switching off is determined solely by the carrier recombination process, neglecting the carrier leakages.

The dynamic behaviour of electron and hole density distributions for low carrier mobility of $\mu_p^{HTL} = \mu_n^{ETL} = 10^{-6}$ cm^2 V^{-1} s^{-1} in HTL and ETL is presented in Fig. 4c and d. When the voltage is switched on (Fig. 4c), the carriers at the HTL and ETL boundaries accumulate slowly due to the low carrier mobilities of the HTL and ETL. This results in a much slower accumulation of the carriers at the QD layer, leading to a delay in emission response [48,71]. When the voltage is switched off (Fig. 4d), the carriers at the HTL and ETL boundaries deplete slowly. However, since the decay of carrier density at QD is determined only by the recombination processes and remains unaffected by the slow depletion effect of the carriers at the HTL and ETL boundaries, the decay speed of carriers is observed to be similar to the case of high HTL/ETL mobility. The simulated carrier densities at the HTL/ETL boundary and at the QD layer over time are plotted in Fig. S5.

The simulated emission intensity over time for different charge injection coefficients under a charge-balanced condition is plotted in Fig. 4e and f. When the mobility of the transport layer is high enough (10^{-3} cm^2 V^{-1} s^{-1}) (Fig. 4e), as the charge injection coefficient increases, higher intensity is observed with faster response time. This is attributed to the larger accumulation of the carriers at the HTL/ETL boundaries as carrier injection sources. However, when the mobility of the transport layer is relatively low (10^{-6} cm^2 V^{-1} s^{-1}) (Fig. 4f), delayed response after the voltage application is observed due to the slow carrier accumulation at the boundaries of HTL and ETL [71]. Therefore, it is confirmed by the dynamic charge transport simulation that higher carrier mobility of the transport layer is required to minimise the delay of the electro-optical response in the QD-LED device.

4.4. Parametric analysis of dynamic behaviour of QD-LED devices

The time-dependent emission responses of QD-LEDs for various charge balance conditions and recombination parameters are presented in Fig. 5. The intensity curves for the time are simulated under pulse voltage. To quantify the charge balance conditions, a band misalignment parameter δ, defined by $\delta = \Delta E_V$ - ΔE_C for the energy band offsets ΔE_V and ΔE_C, is employed in the simulation. Other parameters related to the carrier injection for hole and electron are assumed to be identical. Hence, the charge-balanced condition is represented by $\delta = 0$ eV, while the charge-imbalanced conditions due to the misalignment of the energy band level are described by $\delta > 0$ eV for the electron-rich case.

The dependency of the normalised emission response for the different recombination constants under a charge-balanced condition ($\delta = 0$ eV) is analysed in Fig. 5a–c. In Fig. 5a–as the Langevin recombination strength B increases, a faster on/off response caused by the higher radiative recombination rate is observed. In Fig. 5b–as the SRH recombination frequency A increases, a faster off response is observed due to a higher SRH recombination rate, while the on-response speed is barely changed, reflecting the balance between carrier injection and the recombination process. In contrast, as the Auger recombination probability C increases, faster responses in both on and off switchings are observed by a higher Auger recombination process (Fig. 5c). From the results, it is observed that the response speed increases as the recombination parameters increase. However, the maximum intensity increases as the Langevin radiative recombination strength increases and SRH and Auger non-radiative recombination parameters decrease (Fig. S6). Although the response of the device becomes faster as the A and C parameters increase, these factors inhibit the maximum intensity,

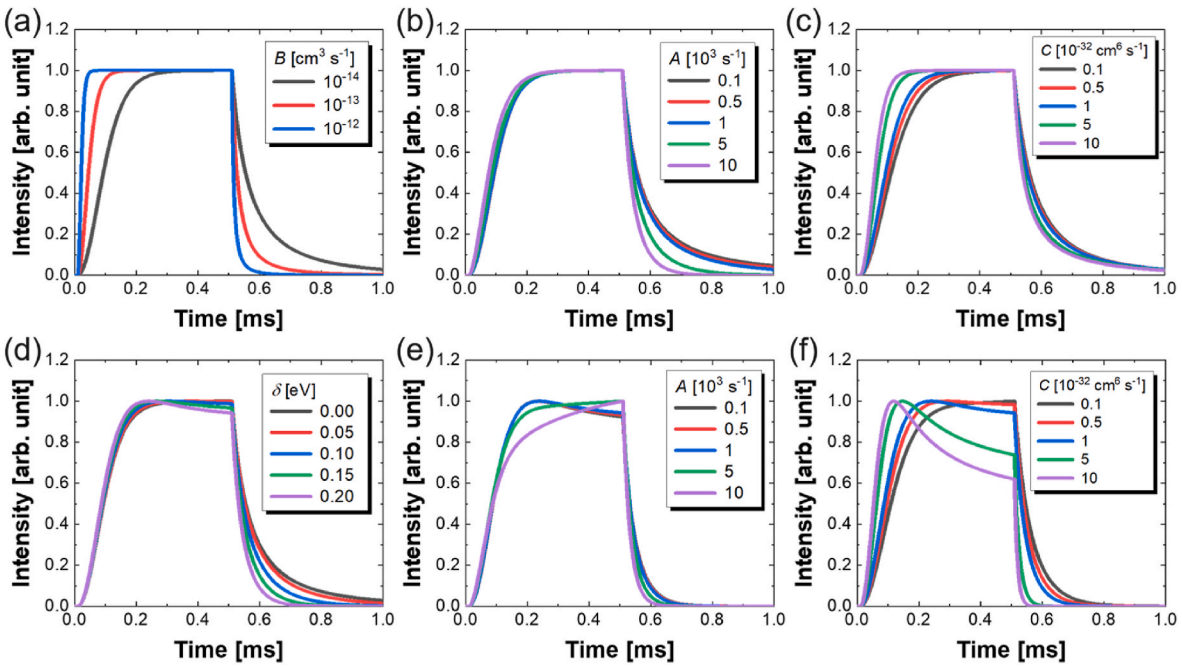

Fig. 5. The time-dependent emission response of QD-LED devices for various charge injection conditions and recombination parameters. The emission response of QD-LED devices under a charge-balanced condition ($\delta = 0$ eV) for (a) different Langevin radiative recombination strength B, (b) SRH non-radiative recombination frequency A, and (c) Auger non-radiative recombination probability C. (d) The emission response of QD-LED devices under different charge balance conditions for the different band misalignment parameter ($\delta = 0$ eV, 0.05 eV, 0.10 eV, 0.15 eV, 0.20 eV), The emission response of the device for (e) different SRH recombination frequency A and (f) Auger non-radiative recombination probability C under the charge-imbalanced condition of $\delta = 0.2$ eV.

thereby deteriorating the device efficiency. Consequently, to achieve QD-LED devices with high intensity and fast response simultaneously, QD materials having extremely large B with low A and C are required.

The response of the QD-LED device for the charge-imbalanced condition is analysed in Fig. 5d–f. In Fig. 5d, the band misalignment parameter δ varies from 0.0 eV to 0.2 eV with a 0.05 eV step. Here, A, B, and C are set to be 10^3 s^{-1}, 10^{-14} cm^3 s^{-1}, and 10^{-32} cm^6 s^{-1}, respectively. The emission intensity increases just after the voltage application and decreases during the pulse width, showing the maximum emission intensity and emission drop at the band misalignment condition. Here, the emission drop increases as the band misalignment parameter δ increases. The increment of the emission intensity at the beginning of voltage application is caused by the predominance of Langevin radiative recombination among the recombination processes (Fig. S7a). Then, due to the decay of minority hole carriers by the recombination processes, the difference in carrier densities increases, causing the increment of the Auger recombination rates (Figs. S7a and b). This induces the emission drop during the pulse width at the band misalignment condition. Therefore, the emission intensities reach their maximum just after the voltage application and then decrease during the pulse width. Here, the maximum intensity also decreases as the band misalignment parameter increases (Fig. S7c). From the result, it is quantitatively validated that the charge balance is a critical condition to prevent emission intensity drop during the voltage application. The response curves for different SRH recombination frequency An under the charge-imbalanced condition at $\delta = 0.2$ eV are presented in Fig. 5e. The intensity drops less during voltage application as the SRH recombination frequency A increases. This is because the minority hole carrier decays more slowly after reaching its maximum carrier densities at higher A values (Fig. S8a). In contrast, as the A increases, the maximum intensity decreases due to significant carrier reduction by a higher SRH recombination process (Fig. S8b).

The response curves for different Auger recombination probabilities under the charge-imbalanced condition at $\delta = 0.2$ eV are presented in Fig. 5f. As the Auger recombination probability C increases, the intensity drop occurs more significantly, amplifying the intensity drop from the charge-imbalanced condition. Moreover, as the C increases, the intensity reaches its maximum more quickly according to the dynamics of minority hole carriers in Fig. S8c. In contrast, maximum intensity decreases as the C increases, due to the lack of hole by non-radiative recombination coupled with the charge-imbalanced condition (Fig. S8d). The discrepancy in intensity drop across both the Cd-based and Cd-free red, green, and blue QD-LEDs from our experiments in Fig. 2 can be explained by the charge imbalance and variations in Auger recombination probability. The misalignment of the energy band between the QDs and the transport layers can cause the charge injection imbalance. The variations in the energy level configuration of the QDs, such as differences in energy bandgap and the edges of the conduction or valence bands, across red, green, and blue colours result in more serious band misalignment resulting in a significant emission intensity drop during the voltage application. It is found from the literature that the Cd-free QD-LEDs can be more balanced than the Cd-based QD-LEDs [6, 72–74]. In detail, the Cd-free QDs can have a higher conduction band level than the Cd-based QD materials, leading to more balance in the band alignment. Therefore, the Cd-based QD-LED devices show a larger emission drop compared with the Cd-free QD-LED devices as shown in Fig. 2. Moreover, this intensity drop is further amplified by the Auger recombination process. The charge balance condition is strongly connected with the hole and electron injection to the QD layer. The mismatch of the hole and electron injection is determined by the difference in band-offsets, tunnelling probabilities, carrier mobilities, electric fields at interfaces of HTL/QD and QD/ETL, and other material properties between HTL and ETL such as carrier mobility, dielectric constant, doping density, etc.

In order to maximise the charge balance in QD-LED devices, experimental attempts are being actively made to achieve charge balance by selecting materials for the transport layers and inserting various interlayers between QD/ETL or QD/HTL [72–74]. To select and guide proper HTL/ETL and QD materials, the influence of various variables such as energy level, mobility, dielectric constant, and effective mass on

dynamic electro-optical characteristics can be comprehensively analysed by simulating electro-optical properties of devices with the QD-specified charge transport model. Especially, when the dielectric constants or mobilities of HTL and ETL are different from each other, the QD-specified charge transport model can guide experiments by proposing the optimal energy level for balancing carrier injection. Especially, if an actual device shows an experimental emission drop, this can be minimised by proper materials or interlayers designed by the charge transport simulation. To achieve this, a more detailed experimental study on the relation between the intensity drops and material properties, including energy band levels and recombination parameters, is required to minimise the intensity drop in QD-LED devices and to enhance their electro-optical properties. We expect that the QD-specified charge transport model is useful not only for predicting but also for analysing and optimizing the experimental electro-optical properties.

4.5. *Space-charge accumulation in QDs after switching off the voltage*

Fig. 6 shows the electrical space charge accumulation mechanism in the QDs after switching off the voltage. The dynamic carrier density at the QD layer under charge-balanced ($\delta = 0$ eV) and electron-rich charge-imbalanced conditions ($\delta = 0.2$ eV) are simulated in Fig. 6a. The electron and hole densities are identical at the charge-balanced condition, while the excessive electron is observed at the electron-rich charge-imbalanced condition due to the lack of hole injection by higher valence band offset compared with the conduction band offset for the electron. The charge densities at the QD layer over time are presented in Fig. 6b. In the charge-balanced condition, the space charge is always neutral at the QD layer due to the identical hole and electron densities. In contrast, the negative space-charge density of -0.21 C cm^{-3} is accumulated at the QDs for the electron-rich charge-imbalanced condition. This indicates that the space charge accumulation at the QDs after switching off the voltage is affected by the charge imbalance between the hole and the electron.

Fig. 6c–f shows the distributions of carriers, charge density, potential, and their corresponding electric field across the device sufficient time after switching off the voltage. In Fig. 6c, under the charge-balanced condition ($\delta = 0$ eV), the electron and hole densities at QDs are identical to around 10^{17} cm^{-3}. The hole density at the HTL/QD boundary and the electron density at the QD/ETL boundary are both approximately 5×10^{13} cm^{-3} at the voltage-off state. In contrast, under the charge-imbalanced condition ($\delta = 0.2$ eV), excessive electrons of 7×10^{17} cm^{-3} density and the minority holes of 2.4×10^{10} cm^{-3} density are accumulated at the QDs even for the voltage off state. Moreover, highly excessive holes are accumulated at the HTL/QD boundary with a density of 4×10^{17} cm^{-3}, while the electron at the ETL/QD boundary is depleted to 8×10^{8} cm^{-3} density, due to the electrical interaction with excessive electrons at the QD layer. In the charge-imbalanced condition, the space charge density at the HTL/QD interface after switching off the voltage is observed to be 0.28 C cm^{-3} due to the excessive accumulation of holes at the HTL/QD interface (Fig. 6d). The distribution of potential and the electric field after switching off the voltage are plotted in Fig. 6e and f. Under the charge-balanced condition, the internal potential within the QDs shows a linear distribution due to the charge neutrality of the QDs. In contrast, under the charge-imbalanced condition, a non-linear potential distribution across the QDs is induced with a stronger localized electric field within the QD layer due to the negatively charged QDs.

The ionised QDs by the excessive electron can attract and react with oxygen and moisture to the QD surface by the localised electric fields, affecting the surface states of the QDs and potentially leading to oxidation or hydrolysis reactions on the QD surface [75–79]. These surface reactions from the ionisation of the QDs after switching off the voltage alter the electro-optical properties of the QDs, degrading the lifetime of the QD-LED devices. The ionisation of the QDs is mainly attributed to the charge imbalance between the hole and electron at the QDs caused by the mismatch of the carrier injections, especially due to the band offset difference between hole and electron injections. From

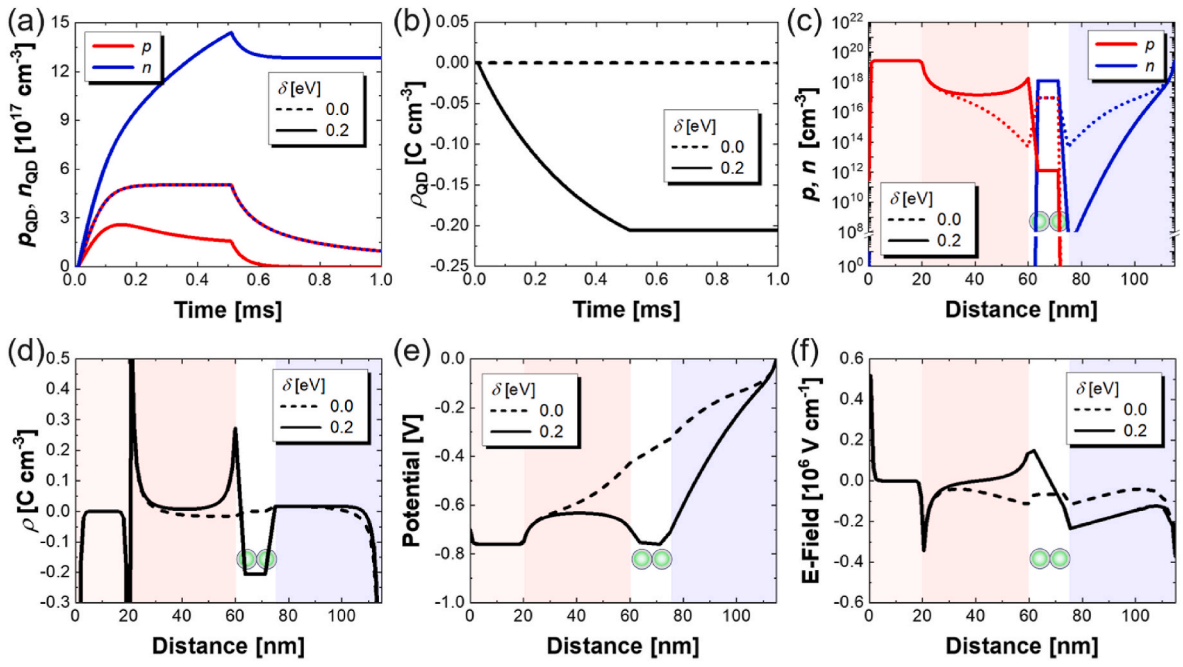

Fig. 6. Electrical space-charge accumulation mechanism in the QD-LED device after switching off the voltage. (a) The dynamic carrier density at the QD layer under charge-balanced ($\delta = 0$ eV) and electron-rich charge-imbalanced conditions ($\delta = 0.2$ eV). (b) The charge densities at the QD layer over time for $\delta = 0$ eV and $\delta = 0.2$ eV. Due to the identical hole and electron densities, the charge is always neutral at the QD layer in the charge-balanced condition. In contrast, the negative space-charge density of -0.21 C cm^{-3} is induced at the QDs for the electron-rich charge-imbalanced condition. The distributions of (c) carriers, (d) space charge density, (e) electric potential, and (f) electric field across the device at sufficient time after switching off the voltage. Under the charge-imbalanced condition, a non-linear potential distribution across the QDs is induced with a stronger localized electric field within the QD layer due to the negatively charged QDs.

the space charge accumulation at the QDs predicted by the charge transport simulation, it is quantitatively revealed that achieving the charge-balanced condition is a key requirement to minimise the degradation of the QD-LEDs and to enhance the lifetimes of the device. Consequently, the QD-specified dynamic charge transport simulation model is useful not only for predicting the transient emission response behaviour of the QD-LED devices but also for designing and optimizing the materials and device configurations to maximise the electro-optical properties and the lifetime of the QD-LED devices. Therefore, this computational approach will pave the way for advancing high-speed, full-colour QD-LED display technologies, thereby contributing to the development of next-generation displays with superior motion picture image quality.

5. Conclusion

We investigated the dynamic emission response of QD-LEDs based on the QD-specified computational charge transport simulation model. From the experiments, the Cd-based QD-LEDs demonstrate fast on and off response times of approximately 0.3 ms and 0.4 ms respectively, while the Cd-free QD-LED devices exhibit slower on and off response times of around 0.4 ms and 0.6 ms, respectively. The emission drop in Cd-based QD-LEDs increases in the order of red (5 %), green (18 %), and blue (54 %) during a 4 ms pulse, while the emission drop decreases in the sequence of red (24 %), green (15 %), and blue (7 %) in Cd-free QD-LEDs.

The experimental on- and off-responses and emission drop of the QD-LED devices were quantitatively analysed by the QD-specified charge transport model for combinatorial carrier recombination processes and different charge balance conditions. As the *A*, *B*, and *C* increase, faster on and off response speeds were observed due to the faster decay of the carriers. An increased carrier injection coefficient also significantly enhances the on-response speed of the QD-LED device. The charge-imbalance condition, especially for the misalignment of the energy band levels, results in a serious intensity drop during the voltage application. The device degradation mechanism of the QD-LEDs was also quantitatively analysed by the dynamic charge transport simulation model. Under charge-imbalanced conditions, the QDs were negatively charged even after switching off the voltage. This space charge accumulation at the QDs causes the device degradation, diminishing its lifetime. Therefore, to achieve a fast response speed without emission intensity drop and a long lifetime, careful design and optimisation of material composition and device configuration based on the QD-specified charge transport model is required. This computational analysis of the transient emission response of the QD-LED will pave the way for advancing high motion picture and colour quality next-generation display technologies with high-speed driving systems based on QD-LED technology.

CRediT authorship contribution statement

Jeong-Wan Jo: Writing – original draft, Visualization, Methodology, Investigation, Formal analysis. **Yoonwoo Kim:** Writing – review & editing, Writing – original draft, Software, Methodology, Data curation. **Bo Hou:** Writing – review & editing, Methodology, Formal analysis. **Sung-Min Jung:** Writing – review & editing, Writing – original draft, Visualization, Software, Methodology, Formal analysis, Data curation, Conceptualization. **Jong Min Kim:** Writing – review & editing, Supervision, Project administration, Methodology, Funding acquisition.

Declaration of competing interest

The authors declare that they have no known competing financial interests or personal relationships that could have appeared to influence the work reported in this paper.

Data availability

Data will be made available on request.

Acknowledgements

This work was supported by the UK Engineering and Physical Sciences Research Council (EPSRC) project ‘Smart Flexible Quantum Dot Lighting’ (Grant No. EP/P027628/1) and by the European Union under H2020 project ‘1D-NEON’ (Grant No. 685758).

Appendix A. Supplementary data

Supplementary data to this article can be found online at https://doi.org/10.1016/j.mtphys.2024.101492.

References

[1] A.I. Ekimov, A.A. Onushchenko, Quantum size effect in three-dimensional microscopic semiconductor crystals, JETP Lett 34 (1981) 345–349, https://doi.org/10.1134/S0021364023130040.
[2] V.L. Colvin, M.C. Schlamp, A.P. Allvlsatos, Light-emitting diodes made from cadmium selenide nanocrystals and a semiconducting polymer, Nature 370 (1994) 354–357, https://doi.org/10.1038/370354a0.
[3] A.P. Alivisatos, Semiconductor clusters, nanocrystals, and quantum dots, Science 271 (1996) 933–937, https://doi.org/10.1126/science.271.5251.933.
[4] J.M. Caruge, J.E. Halpert, V. Wood, V. Bulović, M.G. Bawendi, Colloidal quantum-dot light-emitting diodes with metal-oxide charge transport layers, Nat. Photonics 2 (2008) 247–250, https://doi.org/10.1038/nphoton.2008.34.
[5] Y. Shirasaki, G.J. Supran, M.G. Bawendi, V. Bulović, Emergence of colloidal quantum-dot light-emitting technologies, Nat. Photonics 7 (2013) 13–23, https://doi.org/10.1038/nphoton.2012.328.
[6] P. Kathirgamanathan, L.M. Bushby, M. Kumaraverl, S. Ravichandran, S. Surendrakumar, Electroluminescent organic and quantum dot LEDs: the state of the art, J. Disp. Technol. 11 (2015) 480–493, https://doi.org/10.1109/JDT.2015.2418279.
[7] C.R. Kagan, E. Lifshitz, E.H. Sargent, D.V. Talapin, Building devices from colloidal quantum dots, Science 353 (2016): aac5523, https://doi.org/10.1126/science.aac5523.
[8] X. Dai, Y. Deng, X. Peng, Y. Jin, Quantum-dot light-emitting diodes for large-area displays: towards the dawn of commercialization, Adv. Mater. 29 (2017): 1607022, https://doi.org/10.1002/adma.201607022.
[9] S.Y. Bang, Y.-H. Suh, X.-B. Fan, D.-W. Shin, S. Lee, H.W. Choi, T.H. Lee, J. Yang, S. Zhan, W. Harden-Chaters, C. Samarakoon, L.G. Occhipinti, S.D. Han, S.-M. Jung, J.M. Kim, Technology progress on quantum dot light-emitting diodes for next-generation displays, Nanoscale Horiz 6 (2021) 68–77, https://doi.org/10.1039/D0NH00556H.
[10] D.C. Kim, H. Seung, J. Yoo, J. Kim, H.H. Song, J.S. Kim, Y. Kim, K. Lee, C. Choi, D. Jung, C. Park, H. Heo, J. Yang, T. Hyeon, M.K. Choi, D.-H. Kim, Intrinsically stretchable quantum dot light-emitting diodes, Nat. Electron. 7 (2024) 365–374, https://doi.org/10.1038/s41928-024-01152-w.
[11] X. Shen, A. Kamath, G.-S. Philippe, Mid-infrared cascade intraband electroluminescence with HgSe–CdSe core–shell colloidal quantum dots, Nat. Photonics 17 (2023) 1041–1046, https://doi.org/10.1038/s41566-023-01270-5.
[12] S. Lee, H.W. Choi, C.L. Figueiredo, D.-W. Shin, F.M. Moncunill, K. Ullrich, S. Sinopoli, P. Jovančić, J. Yang, H. Lee, M. Eisenreich, U. Emanuele, S. Nicotera, A. Santos, R. Igreja, A. Marrani, R. Momentè, J. Gomes, S.-M. Jung, S.D. Han, S. Y. Bang, S. Zhan, W. Harden-Chaters, Y.-H. Suh, X.-B. Fan, T.H. Lee, J.-W. Jo, Y. Kim, A. Costantino, V.G. Candel, N. Durães, S. Meyer, C.-H. Kim, M. Lucassen, A. Nejim, D. Jiménez, M. Springer, Y.-W. Lee, G.-H. An, Y. Choi, J.I. Sohn, S. Cha, M. Chhowalla, G.A.J. Amaratunga, L.G. Occhipinti, P. Barquinha, E. Fortunato, R. Martins, J.M. Kim, Truly form-factor–free industrially scalable system integration for electronic textile architectures with multifunctional fiber devices, Sci. Adv. 9 (2023), https://doi.org/10.1126/sciadv.adf4049 eadf4049.
[13] C. Samarakoon, H.W. Choi, S. Lee, X.-B. Fan, D.-W. Shin, S.Y. Bang, J.-W. Jo, L. Ni, J. Yang, Y. Kim, S.-M. Jung, L.G. Occhipinti, G.A.J. Amaratunga, J.M. Kim, Optoelectronic system and device integration for quantum-dot light-emitting diode white lighting with computational design framework, Nat. Commun. 13 (2022) 4189, https://doi.org/10.1038/s41467-022-31853-9.
[14] H.J. Seung, C. Choi, D.C. Kim, J.S. Kim, J.H. Kim, J. Kim, S.I. Park, J.A. Lim, J. Yang, M.K. Choi, T. Hyeon, D.-H. Kim, Integration of synaptic phototransistors and quantum dot light-emitting diodes for visualization and recognition of UV patterns, Sci. Adv. 8 (2022) eabq3101, https://doi.org/10.1126/sciadv.abq3101.
[15] H. Zhang, S. Chen, X.W. Sun, Efficient red/green/blue tandem quantum-dot light-emitting diodes with external quantum efficiency exceeding 21, ACS Nano 12 (2018) 697–704, https://doi.org/10.1021/acsnano.7b07867.
[16] H. Zhang, Q. Su, Y. Sun, S. Chen, Efficient and color stable white quantum-dot light-emitting diodes with external quantum efficiency over 23, Adv. Opt. Mater. 6 (2018): 1800354, https://doi.org/10.1002/adom.201800354.
[17] H. Shen, Q. Gao, Y. Zhang, Y. Lin, Q. Lin, Z. Li, L. Chen, Z. Zeng, X. Li, Y. Jia, S. Wang, Z. Du, L.S. Li, Z. Zhang, Visible quantum dot light-emitting diodes with

simultaneous high brightness and efficiency, Nat. Photonics 13 (2019) 192–197, https://doi.org/10.1038/s41566-019-0364-z.
[18] Y.-H. Won, O. Cho, T. Kim, D.-Y. Chung, T. Kim, H. Chung, H. Jang, J. Lee, D. Kim, E. Jang, Highly efficient and stable InP/ZnSe/ZnS quantum dot light-emitting diodes, Nature 575 (2019) 634–638, https://doi.org/10.1038/s41586-019-1771-5.
[19] S. Kim, J.-A. Kim, T. Kim, H. Chung, S. Park, S.-M. Choi, H.-M. Kim, D.-Y. Chung, E. Jang, Efficient blue-light-emitting Cd-free colloidal quantum well and its application in electroluminescent devices, Chem. Mater. 32 (2020) 5200–5207, https://doi.org/10.1021/acs.chemmater.0c01275.
[20] T. Kim, K.-H. Kim, S. Kim, S.-M. Choi, H. Jang, H.-K. Seo, H. Lee, D.-Y. Chung, E. Jang, Efficient and stable blue quantum dot light-emitting diode, Nature 586 (2020) 385–389, https://doi.org/10.1038/s41586-020-2791-x.
[21] H. Zhang, Q. Su, S. Chen, Suppressing Förster resonance energy transfer in close-packed quantum-dot thin film: toward efficient quantum-dot light-emitting diodes with external quantum efficiency over 21.6, Adv. Opt. Mater. 8 (2020): 1902092, https://doi.org/10.1002/adom.201902092.
[22] W.-C. Chao, T.-H. Chiang, Y.-C. Liu, Z.-X. Huang, C.-C. Liao, C.-H. Chu, C.-H. Wang, H.-W. Tseng, W.-Y. Hung, P.-T. Chou, High efficiency green InP quantum dot light-emitting diodes by balancing electron and hole mobility, Commun. Mater. 2 (2021) 96, https://doi.org/10.1038/s43246-021-00203-5.
[23] Y. Deng, F. Peng, Y. Lu, X. Zhu, W. Jin, J. Qiu, J. Dong, Y. Hao, D. Di, Y. Gao, T. Sun, M. Zhang, F. Liu, L. Wang, L. Ying, F. Huang, Y. Jin, Solution-processed green and blue quantum-dot light-emitting diodes with eliminated charge leakage, Nat. Photonics 16 (2022) 505–511, https://doi.org/10.1038/s41566-022-00999-9.
[24] H. Xu, J. Song, P. Zhou, Y. Song, J. Xu, H. Shen, S. Fang, Y. Gao, Z. Zuo, J.M. Pina, O. Voznyy, C. Yang, Y. Hu, J. Li, J. Du, E.H. Sargent, F. Fan, Dipole–dipole-interaction-assisted self-assembly of quantum dots for highly efficient light-emitting diodes, Nat. Photonics 18 (2024) 186–191, https://doi.org/10.1038/s41566-023-01344-4.
[25] W. Zhang, B. Li, C. Chang, F. Chen, Q. Zhang, Q. Lin, L. Wang, J. Yan, F. Wang, Y. Chong, Z. Du, F. Fan, H. Shen, Stable and efficient pure blue quantum-dot LEDs enabled by inserting an anti-oxidation layer, Nat. Commun. 15 (2024) 783, https://doi.org/10.1038/s41467-024-44894-z.
[26] Y. Gao, B. Li, X. Liu, H. Shen, Y. Song, J. Song, Z. Yan, X. Yan, Y. Chong, R. Yao, S. Wang, L.S. Li, F. Fan, Z. Du, Minimizing heat generation in quantum dot light-emitting diodes by increasing quasi-Fermi-level splitting, Nat. Nanotechnol. 18 (2023) 1168–1174, https://doi.org/10.1038/s41565-023-01441-z.
[27] J. Wang, C. Yuan, S. Chen, Household alternating current electricity plug-and-play quantum-dot light-emitting diodes, Nat. Commun. 15 (2024) 3512, https://doi.org/10.1038/s41467-024-47891-4.
[28] H. Baek, S. Kang, J. Heo, S. Choi, R. Kim, K. Kim, N. Ahn, Y.-G. Yoon, T. Lee, J. B. Chang, K.S. Lee, Y.-G. Park, J. Park, Insights into structural defect formation in individual InP/ZnSe/ZnS quantum dots under UV oxidation, Nat. Commun. 15 (2024) 1671, https://doi.org/10.1038/s41467-024-45944-2.
[29] S. He, X. Tang, Y. Deng, N. Yin, W. Jin, X. Lu, D. Chen, C. Wang, T. S, Q. Chen, Y. Jin, Anomalous efficiency elevation of quantum-dot light-emitting diodes induced by operational degradation, Nat. Commun. 14 (2023) 7785, https://doi.org/10.1038/s41467-023-43340-w.
[30] X. Chen, X. Lin, L. Zhou, X. Sun, R. Li, M. Chen, Y. Yang, W. Hou, L. Wu, W. Cao, X. Zhang, X. Yan, S. Chen, Blue light-emitting diodes based on colloidal quantum dots with reduced surface-bulk coupling, Nat. Commun. 14 (2023) 284, https://doi.org/10.1038/s41467-023-35954-x.
[31] K.-S. Cho, E.K. Lee, W.-J. Joo, E. Jang, T.-H. Kim, S.J. Lee, S.-J. Kwon, J.Y. Han, B.-K. Kim, B.L. Choi, J.M. Kim, High-performance crosslinked colloidal quantum-dot light-emitting diodes, Nat. Photonics 3 (2009) 341–345, https://doi.org/10.1038/nphoton.2009.92.
[32] V. Wood, M.J. Panzer, J. Chen, M.S. Bradley, J.E. Halpert, M.G. Bawendi, V. Bulović, Inkjet-printed quantum dot–polymer composites for full-color AC-driven displays, Adv. Mater. 21 (2009) 2151–2155, https://doi.org/10.1002/adma.200803256.
[33] T.-H. Kim, K.-S. Cho, E.K. Lee, S.J. Lee, J. Chae, J.W. Kim, D.H. Kim, J.-Y. Kwon, G. Amaratunga, S.Y. Lee, B.L. Choi, Y. Kuk, J.M. Kim, K. Kim, Full-colour quantum dot displays fabricated by transfer printing, Nat. Photonics 5 (2011) 176–182, https://doi.org/10.1038/nphoton.2011.12.
[34] T.M. Smeeton, E. Angioni, E.A. Boardman, M. Izumi, N. Iwata, Y. Nakanishi, T. Ishida, 54-1: *Invited paper*: development of electroluminescent QD-LED displays, SID. Int. Symp. Dig. Tec. 50 (2019) 742–745, https://doi.org/10.1002/sdtp.13027.
[35] J. Yang, D. Hahm, K. Kim, S. Rhee, M. Lee, S. Kim, J.H. Chang, H.W. Park, J. Lim, M. Lee, H. Kim, J. Bang, H. Ahn, J.H. Cho, J. Kwak, B. Kim, C. Lee, W.K. Bae, M. S. Kang, High-resolution patterning of colloidal quantum dots via non-destructive, light-driven ligand crosslinking, Nat. Commun. 11 (2020) 2874, https://doi.org/10.1038/s41467-020-16652-4.
[36] Y. Nakanishi, M. Kanehiro, S. Okamoto, K. Matsushita, S. Horiue, H. Utsumi, Y. Qu, X. Fu, K. Konishi, A. Oda, M. Kitagawa, T. Ishida, C. Ippen, D. Barrera, J. DaRos, R. Ma, 8-2: *Invited paper:* development of active-matrix nanoLED display using heavy-metal-free QDs patterned by photolithography process, SID. Int. Symp. Dig. Tec. 53 (2022) 65–68, https://doi.org/10.1002/sdtp.15417.
[37] M. Park, Y.I. Kim, Y.K. Jung, J. Kang, S. Kim, J. Ha, Y. Yoon, C. Lee, All inkjet-printed 6.95″ 217 ppi active matrix QD-LED display with RGB Cd-free QDs in the top-emission device structure, J. Soc. Inf. Disp. 30 (2022) 433–440, https://doi.org/10.1002/jsid.1126.
[38] S. Maeng, S.J. Park, J. Lee, H. Lee, J. Choi, J.K. Kang, H. Cho, Direct photocatalytic patterning of colloidal emissive nanomaterials, Sci. Adv. 9 (2023): eadi6950, https://doi.org/10.1126/sciadv.adi6950.
[39] D. Hahm, J. Lim, H. Kim, J.-W. Shin, S. Hwang, S. Rhee, J.H. Chang, J. Yang, C. H. Lim, H. Jo, B. Choi, N.S. Cho, Y.-S. Park, D.C. Lee, E. Hwang, S. Chung, C.-M. Kang, M.S. Kang, W.K. Bae, Direct patterning of colloidal quantum dots with adaptable dual-ligand surface, Nat. Nanotechnol. 17 (2022) 952–958, https://doi.org/10.1038/s41565-022-01182-5.
[40] T. Meng, Y. Zheng, D. Zhao, H. Hu, Y. Zhu, Z. Xu, S. Ju, J. Jing, X. Chen, H. Gao, K. Yang, T. Guo, F. Li, J. Fan, L. Qian, Ultrahigh-resolution quantum-dot light-emitting diodes, Nat. Photonics 16 (2022) 297–303, https://doi.org/10.1038/s41566-022-00960-w.
[41] R.M.A. Dawson, Z. Shen, D.A. Furst, S. Connor, J. Hsu, M.G. Kane, R.G. Stewart, A. Ipri, C.N. King, P.J. Green, R.T. Flegal, S. Pearson, W.A. Barrow, E. Dickey, K. Ping, S. Robinson, C.W. Tang, S. Van Slyke, F. Chen, J. Shi, M.H. Lu, J.C. Sturm, The impact of the transient response of organic light emitting diodes on the design of active matrix OLED displays, in: International Electron Devices Meeting 1998. Technical Digest (Cat. No.98CH36217), IEEE, San Francisco, CA, USA, 1998, pp. 875–878, https://doi.org/10.1109/IEDM.1998.746494.
[42] X. Xiao, H. Tang, T. Zhang, W. Chen, W. Chen, D. Wu, R. Wang, K. Wang, Improving the modulation bandwidth of LED by CdSe/ZnS quantum dots for visible light communication, Opt Express 24 (2016): 21577, https://doi.org/10.1364/OE.24.021577.
[43] Q. Yuan, X. Guan, X. Xue, D. Han, H. Zhong, H. Zhang, H. Zhang, W. Ji, Efficient $CuInS_2$/ZnS Quantum dots light-emitting diodes in deep red region using PEIE modified ZnO electron transport layer, Physica Status Solidi-R 13 (2019): 1800575, https://doi.org/10.1002/pssr.201800575.
[44] Q. Yuan, T. Wang, P. Yu, H. Zhang, H. Zhang, W. Ji, A review on the electroluminescence properties of quantum-dot light-emitting diodes, Org. Electron. 90 (2021): 106086, https://doi.org/10.1016/j.orgel.2021.106086.
[45] F. Peng, H. Chen, F. Gou, Y.-H. Lee, M. Wand, M.-C. Li, S.-L. Lee, S.-T. Wu, Analytical equation for the motion picture response time of display devices, J. Appl. Phys. 121 (2017): 023108, https://doi.org/10.1063/1.4974006.
[46] Y. Huang, E.-L. Hsiang, M.-Y. Deng, S.-T. Wu, Mini-LED, Micro-LED and OLED displays: present status and future perspectives, Light Sci. Appl. 9 (2020) 105, https://doi.org/10.1038/s41377-020-0341-9.
[47] J. Kim, M. Kim, J.-M. Kim, S.-R. Kim, S.-W. Lee, Driving technology for improving motion quality of active-matrix organic light-emitting diode display, Opt. Eng. 53 (2014): 093105, https://doi.org/10.1117/1.OE.53.9.093105.
[48] C. Blauth, P. Mulvaney, T. Hirai, Transient overshoot and storage of charge carriers on ligands in quantum dot LEDs, J. Appl. Phys. 126 (2019): 075501, https://doi.org/10.1063/1.5100195.
[49] J.-M. Lee, C.H. Kang, J.S. Yoo, H.W. Hwang, S.K. Hong, Y.M. Ha, H.C. Choi, B.-K. Ju, LTPS pixel driving scheme to improve motion blur for AMOLED displays, IEEE Trans. Electron. Dev. 69 (2022) 4950–4957, https://doi.org/10.1109/TED.2022.3189947.
[50] R. Yu, F. Yin, C. Pu, D. Zhou, W. Ji, On the electroluminescence overshoot of quantum-dot light-emitting diodes, Opt. Lett. 48 (2023) 3059, https://doi.org/10.1364/OL.492710.
[51] J.-S. Yoon, B.-W. Kang, B.-S. Kim, C.-H. Oh, B.-C. Ahn, New pixel structure with high G-to-G response time for large size and high resolution OLED TVs, SID Symp. Dig. Tech. Papers (2013) 1010–1013, https://doi.org/10.1002/j.2168-0159.2013.tb06393.x.
[52] Y.-H. Lee, F. Peng, S.-T. Wu, Fast-response switchable lens for 3D and wearable displays, Opt Express 24 (2016) 1668, https://doi.org/10.1364/OE.24.001668.
[53] Y.-H. Lee, G. Tan, K. Yin, T. Zhan, S.-T. Wu, Compact see-through near-eye display with depth adaption, J. Soc. Inf. Disp. 26 (2018) 64–70, https://doi.org/10.1002/jsid.635.
[54] S. Liu, Y. Li, P. Zhou, Q. Chen, Y. Su, Reverse-mode PSLC multi-plane optical see-through display for AR applications, Opt Express 26 (2018) 3394, https://doi.org/10.1364/OE.26.003394.
[55] Q. Chen, Z. Peng, Y. Li, S. Liu, P. Zhou, J. Gu, J. Lu, L. Yao, M. Wang, Y. Su, Multi-plane augmented reality display based on cholesteric liquid crystal reflective films, Opt Express 27 (2019): 12039, https://doi.org/10.1364/OE.27.012039.
[56] J. Piprek, in: Carrier transport, Semiconductor Optoelectronic Devices, Elsevier, 2003, pp. 49–82, https://doi.org/10.1016/B978-0-08-046978-2.50028-4.
[57] J. Piprek, Efficiency droop in nitride-based light-emitting diodes, Phys. Status Solidi A 207 (2010) 2217–2225, https://doi.org/10.1002/pssa.201026149.
[58] S. Karpov, ABC-model for interpretation of internal quantum efficiency and its droop in III-nitride LEDs: a review, Opt. Quant. Electron. 47 (2015) 1293–1303, https://doi.org/10.1007/s11082-014-0042-9.
[59] S. Roy, A.S. Sharbirin, Y. Lee, W.B. Kim, T.S. Kim, K. Cho, K. Kang, H.S. Jung, J. Kim, Measurement of quantum yields of monolayer TMDs using dye-dispersed PMMA thin films, Nanomaterials 10 (2020) 1032, https://doi.org/10.3390/nano10061032.
[60] Y. Kim, J.-W. Jo, J. Yang, Y. Bernstein, S. Lee, S.-M. Jung, J.M. Kim, Computational characterization of quantum-dot light-emitting diodes by combinatorial exciton recombination parameters and photon extraction efficiency, Adv. Opt. Mater. 12 (2024) 2302593, https://doi.org/10.1002/adom.202302593.
[61] X. Gao, S.S. Yee, Hole capture cross section and emission coefficient of defect centers related to high-field-induced positive charges in SiO2 layers, Solid State Electron. 39 (1996) 399–403, https://doi.org/10.1016/0038-1101(95)00128-X.
[62] D. Berner, H. Houili, W. Leo, L. Zuppiroli, Insights into OLED functioning through coordinated experimental measurements and numerical model simulations, Phys. Status Solidi A 202 (2005) 9–36, https://doi.org/10.1002/pssa.200406905.
[63] T. Goudon, V. Miljanović, C. Schmeiser, On the shockley–read–Hall model: generation-recombination in semiconductors, SIAM J. Appl. Math. 67 (2007) 1183–1201, https://doi.org/10.1137/060650751.
[64] G.A.H. Wetzelaer, M. Kuik, H.T. Nicolai, P.W.M. Blom, Trap-assisted and Langevin-type recombination in organic light-emitting diodes, Phys. Rev. B 83 (2011): 165204, https://doi.org/10.1103/PhysRevB.83.165204.

[65] B. Kumar, S.A. Campbell, P. Paul Ruden, Modeling charge transport in quantum dot light emitting devices with NiO and ZnO transport layers and Si quantum dots, J. Appl. Phys. 114 (2013): 044507, https://doi.org/10.1063/1.4816680.
[66] V.P. Sirkeli, O. Yilmazoglu, F. Küppers, H.L. Hartnagel, Effect of p-NiO and n-ZnSe interlayers on the efficiency of p-GaN/n-ZnO light-emitting diode structures, Semicond. Sci. Technol. 30 (2015): 065005, https://doi.org/10.1088/0268-1242/30/6/065005.
[67] F. Vahabzad, A. Rostami, M. Dolatyari, G. Rostami, I.S. Amiri, Solution-processed QD-LEDs in visible range: modulation bandwidth enhancement, Physica B 574 (2019): 411667, https://doi.org/10.1016/j.physb.2019.411667.
[68] S.-M. Jung, T.H. Lee, S.Y. Bang, S.D. Han, D.-W. Shin, S. Lee, H.W. Choi, Y.-H. Suh, X.-B. Fan, J.-W. Jo, S. Zhan, J. Yang, C. Samarakoon, Y. Kim, L.G. Occhipinti, G. Amaratunga, J.M. Kim, Modelling charge transport and electro-optical characteristics of quantum dot light-emitting diodes, npj Comput. Mater. 7 (2021) 122, https://doi.org/10.1038/s41524-021-00591-9.
[69] D. Bera, L. Qian, T.-K. Tseng, P.H. Holloway, Quantum dots and their multimodal applications: a review, Materials 3 (2010) 2260, doi:10.3390/ma3042260.
[70] H.S. Mansur, Quantum dots and nanocomposites, Wiley Interdiscip. Rev. Nanomed. Nanobiotechnol. 2 (2010) 113, https://doi.org/10.1002/wnan.78.
[71] S. Barth, P. Müller, H. Riel, P.F. Seidler, W. Rieß, H. Vestweber, H. Bässler, Electron mobility in tris(8-hydroxy-quinoline)aluminum thin films determined via transient electroluminescence from single- and multilayer organic light-emitting diodes, J. Appl. Phys. 89 (2001) 3711–3719, https://doi.org/10.1063/1.1330766.
[72] T. Lee, D. Hahm, K. Kim, W.K. Bae, C. Lee, J. Kwak, Highly efficient and bright inverted top-emitting InP quantum dot light-emitting diodes introducing a hole-suppressing interlayer, Small 15 (2019): 1905162, https://doi.org/10.1002/smll.201905162.
[73] J. Song, O. Wang, H. Shen, Q. Lin, Z. Li, L. Wang, X. Zhang, L.S. Li, Over 30% external quantum efficiency light-emitting diodes by engineering quantum dot-assisted energy level match for hole transport layer, Adv. Funct. Mater. 29 (2019): 1808377, https://doi.org/10.1002/adfm.201808377.
[74] K. Kim, D. Hahm, G.W. Baek, T. Lee, D. Shin, J. Lim, W.K. Bae, J. Kwak, Effect of excess carriers on the degradation of InP-based quantum-dot light-emitting diodes, ACS Appl. Electron. Mater. 4 (2022) 6229–6236, https://doi.org/10.1021/acsaelm.2c01351.
[75] C. Coburn, S.R. Forrest, Effects of charge balance and exciton confinement on the operational lifetime of blue phosphorescent organic light-emitting diodes, Phys. Rev. Appl. 7 (2017): 041002, https://doi.org/10.1103/PhysRevApplied.7.041002.
[76] S. Chen, W. Cao, T. Liu, S.-W. Tsang, Y. Yang, X. Yan, L. Qian, On the degradation mechanisms of quantum-dot light-emitting diodes, Nat. Commun. 10 (2019) 765, https://doi.org/10.1038/s41467-019-08749-2.
[77] D.S. Chung, T. Davidson-Hall, H. Yu, F. Samaeifar, P. Chun, Q. Lyu, G. Cotella, H. Aziz, Significant enhancement in quantum-dot light emitting device stability *via* a ZnO:polyethylenimine mixture in the electron transport layer, Nanoscale Adv. 3 (2021) 5900–5907, https://doi.org/10.1039/D1NA00561H.
[78] D.S. Chung, T. Davidson-Hall, G. Cotella, Q. Lyu, P. Chun, H. Aziz, Significant lifetime enhancement in QLEDs by reducing interfacial charge accumulation via fluorine incorporation in the ZnO electron transport layer, Nano-Micro Lett. 14 (2022) 212, https://doi.org/10.1007/s40820-022-00970-x.
[79] M. Azadinia, P. Chun, Q. Lyu, G. Cotella, H. Aziz, Differences in electron and hole injection and Auger recombination between red, green, and blue CdSe-based quantum dot light emitting devices, ACS Nano (2024), https://doi.org/10.1021/acsnano.3c07999.